Investigation of the mechanics of intersonic crack propagation along a bimaterial interface using coherent gradient sensing and photoelasticity

By Raman P. Singh[1], John Lambros[2], Arun Shukla[3] and Ares J. Rosakis[1]

[1]*Graduate Aeronautical Laboratories, California Institute of Technology, Pasadena, CA 91125, USA*

[2]*Department of Mechanical Engineering, University of Delaware, Newark, DE 19716, USA*

[3]*Dynamic Photomechanics Laboratory, Department of Mechanical Engineering, University of Rhode Island, Kingston, RI 02881, USA*

This paper describes the first experimental observations of various phenomena characteristic of dynamic intersonic decohesion of bimaterial interfaces. Two separate but complementary optical methods are used in conjunction with high speed photography to explore the nature of the large scale contact and mach wave formation at the vicinity of running cracks in two different bimaterial systems. Theoretical predictions of crack-tip speed regimes where large scale contact is implied are confirmed. Also, the theoretically predicted mach wave emanating from the intersonically propagating crack-tip is observed. Direct visual evidence is also obtained for *another* travelling mach wave emanating from the end of the intersonically moving contact zone.

1. Introduction

In homogeneous materials, the observations of crack growth speeds greater than the shear wave speed, $v > c_s$, is limited to the cases when the loading is applied directly to the propagating crack-tip. For remotely loaded cracks, energy considerations make it impossible for the crack-tip speed to exceed the Rayleigh wave speed of the material (Broberg 1960; Freund 1990). Thus, the only experimental observations of intersonic or supersonic crack-tip speeds, $v > c_s$ or $v > c_l$, in a laboratory setting have been on crack growth along weak crystal planes in single crystals of potassium chloride, where the crack faces were loaded by laser induced expanding plasma (Winkler *et al.* 1970; Curran *et al.* 1970). Indirect observation of intersonic shear rupture ($c_s < v < c_l$) has also been reported for crustal earthquakes (Archuleta 1982). These observations have motivated extensive theoretical work in the area of high-speed shear fracture in homogeneous materials. This has been primarily conducted with seismological applications in mind and includes the work of Burridge (1973), Burridge *et al.* (1979), Freund (1979), Broberg (1985, 1989), Bykovtsev & Kramarovskii (1989) and Aleksandrov & Smetanin (1990).

In bimaterial systems, however, it has been recently demonstrated (by the authors

Proc. R. Soc. Lond. A (1997) **453**, 2649–2667

Printed in Great Britain

TEX Paper

and their co-workers) that intersonic crack propagation along bimaterial interfaces is possible even under remote loading conditions (Liu *et al.* 1993; Lambros & Rosakis 1995*a*, *b*, *c*; Singh & Shukla 1996). Indeed, it has been experimentally shown that if there exists a significant mismatch in the stress wave speeds across the bimaterial interface then the crack can propagate intersonically with respect to the material with the lower shear wave speed, while it remains subsonic with respect to the material with the higher wave speed. Under these conditions only a *finite amount* of energy has to be supplied to the crack-tip to maintain extension as the propagational speed approaches the lower of the two Rayleigh wave speeds. This fact was analytically derived by Yang *et al.* (1991) on the basis of a subsonic analysis and removes the theoretical restriction for the attainment of intersonic crack-tip speeds of the type that exist in homogeneous materials.

Despite these initial attempts, the phenomenon of intersonic crack propagation is still more or less unexplored. The experimental evidence is quite limited and still there does not exist a completely physically realistic theoretical model for the intersonically propagating interfacial crack. In view of these limitations, the current study presents valuable experimental observations on interface failure in the intersonic regime and interprets these observations based on currently available theory.

2. Experimental techniques

The two techniques of coherent gradient sensing (CGS) and photoelasticity were employed independently to study intersonic crack propagation along a bimaterial interface subjected to impact loading. Both these optical techniques provide real-time full field information and are ideally suited to investigate dynamic fracture events when used in conjunction with high speed photography. However, the two techniques have their own advantages and limitations and the information provided is complementary. Hence, employing both the techniques allows for a better understanding of the dynamic fracture process. This will become apparent when the two techniques are discussed in the following sections.

(*a*) *Coherent gradient sensing interferometer (CGS)*

Figure 1 shows a schematic of the CGS setup in a transmission configuration. A coherent monochromatic collimated laser beam is incident on the bimaterial specimen. After transmission through the transparent side of the deforming specimen, it acquires an optical path difference and loses collimation. The optical path difference acquired is due to stress-induced differences in refractive index and due to a non-uniform contraction in the thickness direction around the vicinity of the crack-tip (Poisson's ratio effect for elastic solids). The resulting, non-collimated, beam passes through two line diffraction gratings G_1 and G_2 of fine pitch p (typically 40 lines mm^{-1}). The gratings are situated a distance Δ (typically 30–50 mm) apart and perform a 'shearing' of the incident wave front. The gratings' output intensity is transmitted through a filtering lens L. A diffraction spot pattern is obtained on the filtering plane, which is located at the back focal plane of lens L. At this plane all but one diffraction orders are blocked. The one remaining diffraction spot (either of ± 1 orders), shown in figure 1 as the open circle on the filtering plane, is imaged to produce an interference pattern. For the case of a dynamic experiment the imaging device is a high-speed camera focused on the specimen.

The details of analysing the CGS optical method can be found in several previous

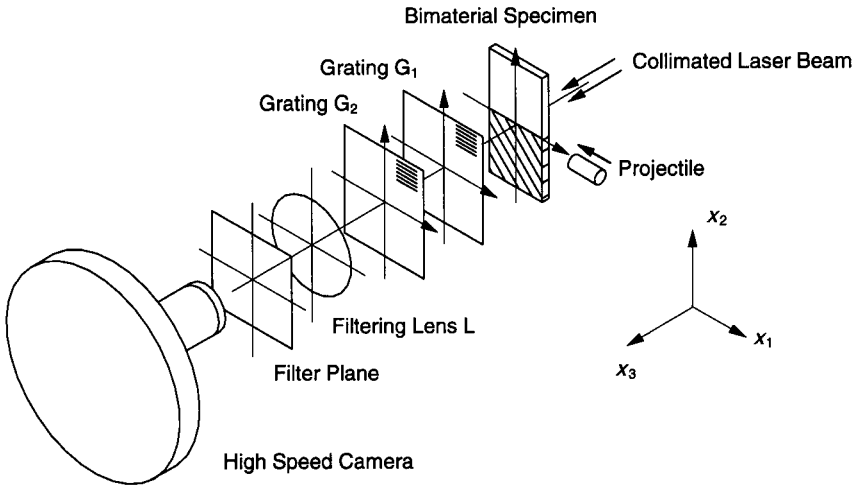

Figure 1. Schematic of CGS setup in transmission. PMMA/steel bimaterial specimen is illustrated.

articles including Tippur *et al.* (1991) and Rosakis (1993) and will not be repeated here for the sake of brevity. The condition for formation of constructive CGS interference fringes on the image plane, for gratings with lines parallel to the x_2-direction, is

$$\frac{\partial(S(x_1,x_2))}{\partial x_1}=\frac{mp}{\Delta},\quad m=0,\pm1,\pm2,\ldots, \tag{2.1}$$

where, $S(x_1,x_2)$ is the optical path change that is introduced due to specimen deformation at a certain location in the x_1–x_2 plane. It has also been assumed that the diffraction gratings G_1 and G_2 are close enough and/or fine enough to obtain an interferogram that represents the x_1 gradient of S, rather than an x_1-finite difference of S. If the grating lines are parallel to the x_1-direction then it can be shown that the condition for constructive interference becomes

$$\frac{\partial(S(x_1,x_2))}{\partial x_2}=\frac{np}{\Delta},\quad n=0,\pm1,\pm2,\ldots. \tag{2.2}$$

For the case of plane stress and a transmission configuration the quantity $S(x_1,x_2)$ is related to the stress state in the deforming specimen as (Rosakis 1993)

$$S(x_1,x_2)\cong c_\sigma h[\hat{\sigma}_{11}(x_1,x_2)+\hat{\sigma}_{22}(x_1,x_2)], \tag{2.3}$$

where c_σ is the stress optical coefficient for the material, h is the specimen thickness and $\hat{\sigma}_{11}$ and $\hat{\sigma}_{22}$ are thickness averages of the in-plane stress components in the plate.

For points outside the near-tip three-dimensional region the CGS patterns assume a simple interpretation in terms of two-dimensional stress field approximations. In particular, equations (2.1) and (2.2) in conjunction with equation (2.3) now indicate that the fringes obtained from regions surrounding the three-dimensional zone can be related to the in-plane gradients of $\hat{\sigma}_{11}+\hat{\sigma}_{22}$ as follows:

$$c_\sigma h\frac{\partial(\hat{\sigma}_{11}+\hat{\sigma}_{22})}{\partial x_1}=\frac{mp}{\Delta},\quad c_\sigma h\frac{\partial(\hat{\sigma}_{11}+\hat{\sigma}_{22})}{\partial x_2}=\frac{np}{\Delta},\quad m,n=0,\pm1,\pm2,\ldots, \tag{2.4}$$

where, in the case of transmission, c_σ is the stress optical coefficient of the transparent material.

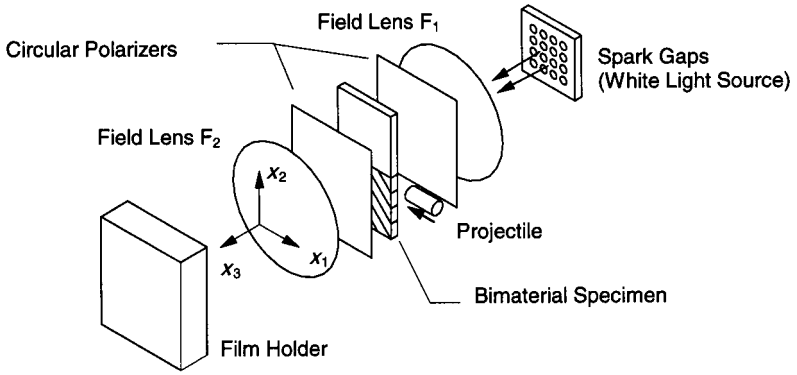

Figure 2. Schematic of photoelasticity setup in transmission. Homalite-100/aluminum bimaterial specimen is illustrated.

The CGS interferograms are imaged by a rotating mirror-type high-speed camera (Cordin Co., model 330A). The camera records 80 frames of the dynamic event and is typically operated at an interframe time of 1.2 μs (about 840 000 frames s^{-1}). Individual frames are obtained by operating the laser light source (Spectra-Physics Argon-ion laser, model 166-09; operating wavelength $\lambda = 514.5$ nm) in a pulsed mode. The exposure time used in all experiments (i.e. the laser pulse duration) is 30 ns and the image is recorded on 35 mm black and white film (Kodak TMAX-3200).

Note that in this case the CGS interferograms represent contours of constant gradients of the first stress invariant, $\hat{\sigma}_{11} + \hat{\sigma}_{22}$, of the thickness averaged stress tensor in plane stress, $\hat{\boldsymbol{\sigma}}$. This invariant can also be expressed in terms of the principal stresses of $\hat{\boldsymbol{\sigma}}$ as follows: $\hat{\sigma}_{11} + \hat{\sigma}_{22} = \hat{\sigma}_1 + \hat{\sigma}_2$, since $\hat{\sigma}_{33} = \hat{\sigma}_3 = 0$. Thus, the technique of CGS will not be sensitive to changes in the individual components of stress as long as the derivative of $\hat{\sigma}_1 + \hat{\sigma}_2$ remains a constant.

(*b*) *Photoelasticity*

A schematic of the photoelastic setup in a transmission configuration is shown in figure 2. The specimen is placed in the optical bench of a high speed Cranz–Schardin spark-gap camera. The optical setup consists of two field lenses, F_1 and F_2, and two circular polarizers, C_1 and C_2. The first field lens, F_1, collimates white light from the spark gaps that is incident on the specimen, while the second field lens, F_2, focuses the light transmitted through the specimen onto the film plane of the high-speed camera. Meanwhile, the two circular polarizers form a circular polariscope, which allows photoelasticity to be used to observe the state of stress in the specimen. The transparent side of the bimaterial specimen is specially chosen so that it exhibits stress induced birefringence, which is a fundamental requirement of this technique. A filter (Kodak Wratten filter no. 8) is placed before the film plane of the high-speed camera, so that only fringes corresponding to a particular wavelength of light are recorded. The technique of photoelasticity is very well established for a variety of solid mechanics applications and the reader is referred to Dally & Riley (1991) for further details.

The generation of isochromatic fringe patterns is governed by the stress optic law. For the case of monochromatic light, the condition for the formation of fringes is expressed as

$$\hat{\sigma}_1 - \hat{\sigma}_2 = N f_\sigma / h, \tag{2.5}$$

where, $\hat{\sigma}_1 - \hat{\sigma}_2$ is the principal stress difference of the thickness averaged stress tensor, $\hat{\boldsymbol{\sigma}}$, f_σ is the material fringe value, h is the specimen thickness and N is the isochromatic fringe order. The isochromatic fringe patterns observed are contours of constant maximum shear stress, $\tau_{\max} = \frac{1}{2}(\hat{\sigma}_1 - \hat{\sigma}_2)$.

The photoelastic fringe patterns are imaged using a high speed Cranz–Schardin spark-gap camera. The camera provides a total of 20 images of the dynamic fracture event at an interframe time of 4 μs (250 000 frames s^{-1}). The spark gaps serve as the light sources and the exposure time is typically 400 ns, as determined by the time duration of the sparks. The recording medium is once again black and white photographic film (Kodak Professional 8" × 10" film no. 4127).

(*c*) *Bimaterial specimen and loading arrangement*

The bimaterial specimens used in these experiments consisted of a transparent polymer bonded directly to a metal. The material combinations were chosen so that there would be a large mismatch in the mechanical properties across the interface and this would intensify the dynamic effects. The particular choice of the transparent polymer was also dictated by the particular needs of the experimental technique employed, i.e. CGS or photoelasticity. For the case of CGS, the transparent half was Plexiglas (Poly-methylmethacrylate or PMMA) while the metal half was AISI 4340 steel. For the photoelastic experiments, the transparent half was Homalite-100, a polyester resin that exhibits stress induced birefringence, while the metal half was 6061 aluminum. Throughout this paper, the transparent polymer side of the specimen will be refered to as material 1 and the metal side as material 2.

Mechanical properties of the material constituents are listed in table 1. Since both PMMA and Homalite-100 exhibit rate sensitivity their properties are listed for two extreme strain rates ($\dot{\varepsilon} = 10^{-3}\,\mathrm{s}^{-1}$ and $\dot{\varepsilon} = 10^{3}\,\mathrm{s}^{-1}$ (glassy state)) that could be encountered by material elements in the vicinity of the propagating crack-tip. In reality the material surrounding the propagating crack-tip is not subject to any uniform value of strain rate. Instead there is a strain rate distribution around the crack-tip which depends on the crack-tip stress field. Thus, the material wave speeds at any given point of observation would depend on the effective strain rate at that point and would lie between the two extreme values listed in table 1. It should be noted that neither 6061 aluminum nor 4340 steel exhibit any appreciable strain rate sensitivity for the strain rates in consideration.

As shown in table 1, either of the PMMA/steel or the Homalite-100/aluminum combinations result in a significant mismatch of mechanical properties and, most importantly for dynamics, wave speeds across the bimaterial interface. The values of the plane-stress quasi-static oscillatory index, ε, are also listed for PMMA/steel, PMMA/rigid, Homalite-100/aluminum and Homalite-100/rigid material combinations. As demonstrated by these values, both the material combinations behave very similarly to an elastic/rigid bimaterial system. Thus, one can expect intensified interfacial effects during the dynamic fracture event.

The specimen preparation procedure for both the material combinations is the same in principle. The bonding is achieved using the monomer of the transparent polymer in conjunction with appropriate catalysts/hardening agents. Bonding for the PMMA/steel interface is described by Tippur & Rosakis (1991) while that for the Homalite-100/aluminum interface by Singh & Shukla (1996). The issue of bond strength and toughness has also been addressed by the same authors.

The bimaterial specimens were subjected to one-point bend-type impact loading

Table 1. *Mechanical properties and wave speeds of interface constituents*
($A = 10^{-3}\ \mathrm{s}^{-1}$, $B = 10^{3}\ \mathrm{s}^{-1}$, $\varepsilon^{\mathrm{Homalite-100/aluminum}} = 0.0912$, $\varepsilon^{\mathrm{Homalite-100/rigid}} = 0.1073$ $\varepsilon^{\mathrm{PMMA/steel}} = 0.1037$, $\varepsilon^{\mathrm{PMMA/rigid}} = 0.1073$.)

	PMMA		Homalite-100[a]			
property	$\dot{\varepsilon} = A$	$\dot{\varepsilon} = B$	$\dot{\varepsilon} = A$	$\dot{\varepsilon} = B$	4340 steel	6061 aluminum
Young's modulus, E (GPa)	3.2	5.6	3.9	5.3	208	71
Poisson's ratio, ν	0.35	0.35	0.35	0.35	0.3	0.33
density, ρ (kg m^{-3})	1190	1190	1230	1230	7830	2770
dilatational wave speed, c_1 (m s^{-1})	1760	2330	1890	2220	5400	5430
(plane stress)						
shear wave speed, c_s (m s^{-1})	1000	1330	1080	1270	3195	3100
Rayleigh wave speed, c_R (m s^{-1})	935	1243	1010	1185	2950	2890
material fringe value, f_σ (kN m^{-1})	—	—	—	23.7	—	—

[a]Manufactured by Homalite Inc., Delaware, USA.

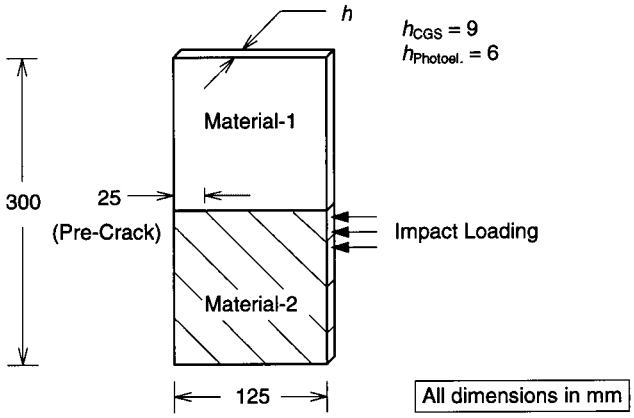

Figure 3. Bimaterial specimen showing the one point bend impact geometry.

as shown in figure 3. The impact was achieved by using a cylindrical steel projectile launched using a pressurized gas-gun. For the CGS experiments the projectile was 75 mm long and 50 mm in diameter, and the impact velocity was 20 m s^{-1}. Meanwhile, for the photoelastic experiments the projectile was 100 mm long and 12.5 mm in diameter, and the impact velocity was 30 m s^{-1}. As will be shown later, both these loadings result in essentially the same mode of bimaterial failure. It is apparent that the loading history experienced by the crack-tip would depend on whether the specimen was impacted on the polymer side or the metal side of the interface. In all these experiments the specimen was impacted from the metal side of the interface, so that the energy to the propagating crack-tip would be supplied from the side with the higher stress-wave speeds.

The nature of the loading arrangement results in the interface crack-tip being loaded primarily in shear. The projectile impacting the metal side of the specimen generates stress wave fronts as shown in figure 4*a*. The main compressive dilatation-

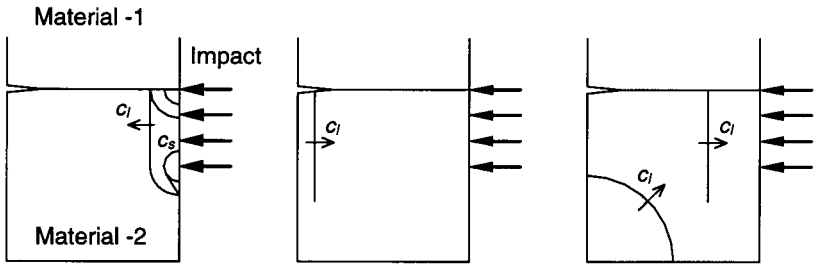

Figure 4. Stress wave loading of the interfacial crack-tip arising from the one point bend impact: (*a*) just after impact; (*b*) just before initiation; and (*c*) during crack growth.

al stress wave traverses the width of the metal specimen. When this wave passes by the precrack-tip at the interface it loads the crack-tip primarily in shear. This compressive dilatational stress wave then reflects from the opposite free surface as a tensile wave and again propagates by the crack-tip on the interface going in the opposite direction. Doing so it enhances the state of shear that exists around the crack-tip (doubles the particle velocity in the negative x_1-direction), resulting in crack initiation and crack extension. The acoustic mismatch across the bimaterial interface greatly impedes the transfer of stress waves from the metal to the polymer. Hence, the interface crack is driven from the metal side and primarily in a state of shear. Note that, at later times, other reflections from the specimen boundaries will also impinge upon the interface, as shown in figure 4*c*, and will change the nature of loading. However, these effects occur later on in the time history of the fracture process.

3. Results and discussion

(*a*) *Observation of contact and line-of-discontinuity*

A typical selected sequence of CGS interferograms from a one point bend experiment on a PMMA/steel specimen is shown in figure 5. Note that the CGS fringes are observed only in the transparent side (i.e. the PMMA side) of the specimen. The instantaneous location of the crack-tip is known from each frame and this was used to determine the history of the crack-tip speed. A typical crack-tip speed history obtained from one such experiment is plotted in figure 6. The shear wave speed of PMMA, c_s^{PMMA}, is also plotted in the same figure for two extreme loading rates ($\dot{\varepsilon} = 10^{-3}\,\mathrm{s}^{-1}$ and $\dot{\varepsilon} = 10^{3}\,\mathrm{s}^{-1}$ (glassy state)) that may be typically expected in the region surrounding the propagating crack-tip. The effective shear wave speed at a given point of observation would depend on the effective strain rate at that point and thus would lie between the two extreme values shown in figure 6. After initiation the crack-tip accelerated very rapidly to beyond the upper extreme of the shear wave speed of PMMA. Then the crack-tip speed oscillated between the upper and lower extremes of c_s^{PMMA} for about 15 μs, after which it accelerated even further. Recent experiments have confirmed this trend and have shown crack-tip speeds approaching $\sqrt{2}$ times the upper extreme of c_s^{PMMA} (Rosakis and co-workers, unpublished research). Crack-tip accelerations were of the order of $10^8\,\mathrm{m\,s}^{-2}$, which establishes the highly unstable nature of this crack-tip event. This dynamic and highly repeatable variation of the crack-tip speed was first observed by Lambros & Rosakis (1995*a*) and explained by Lambros & Rosakis (1995*c*) and Liu *et al.* (1995).

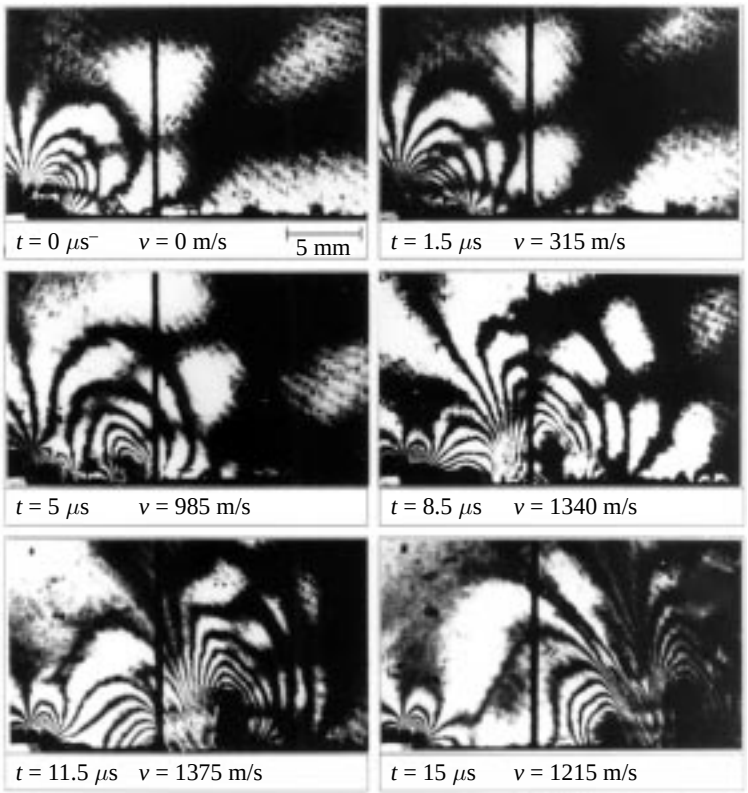

Figure 5. Typical set of CGS interferograms obtained for dynamic crack growth along a PMMA/steel bimaterial interface subjected to impact loading.

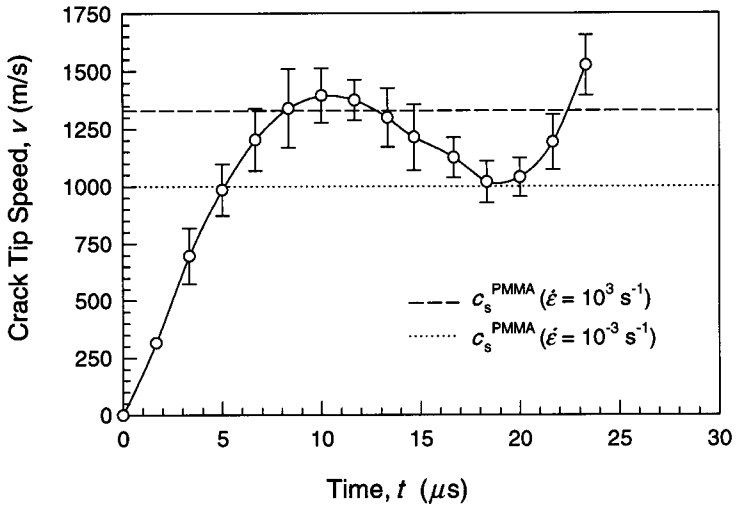

Figure 6. Typical crack-tip speed history for dynamic crack growth along a PMMA/steel bimaterial interface subjected to impact loading.

Tests conducted with Homalite-100/aluminum specimens, using the technique of photoelasticity, yield similar observations despite the fact that now different materials

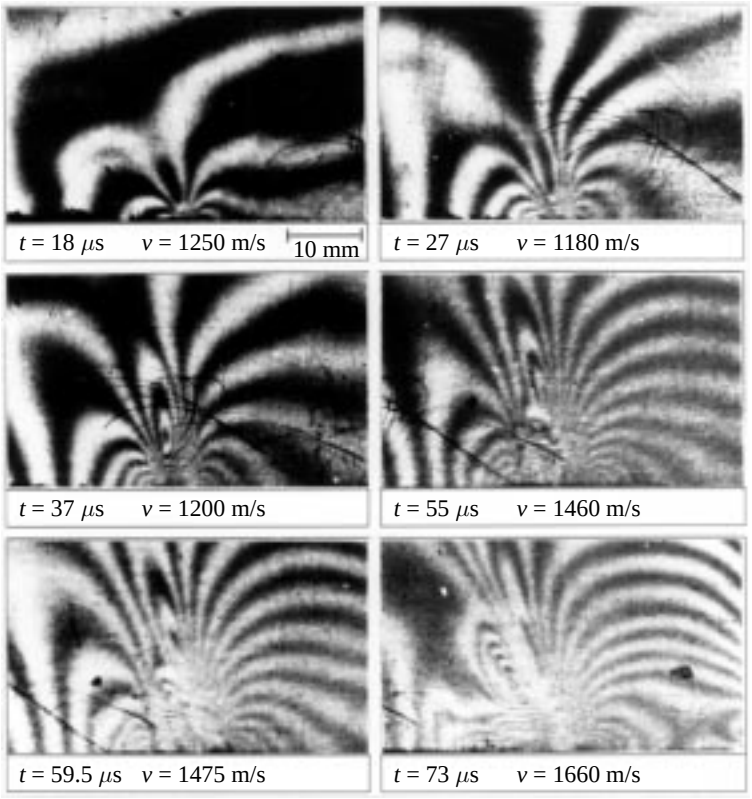

Figure 7. Typical set of isochromatic fringe patterns obtained for dynamic crack growth along a Homalite-100/aluminum bimaterial interface subjected to impact loading.

constitute the bimaterial interface. Figure 7 shows a typical set of isochromatic fringe patterns obtained for dynamic crack propagation along a Homalite-100/aluminum bimaterial interface. The history of the crack-tip speed typically observed for these experiments is plotted in figure 8. As observed for the PMMA/steel case the crack-tip accelerated very rapidly after initiation to beyond the upper extreme of the shear wave speed of material 1 (Homalite-100). Thereafter, the crack-tip speed stayed at this value for about 20 μs, after which it accelerated even further.

The terminal crack-tip speeds that have been observed for these experiments were about 140% of the upper extreme of $c_{\mathrm{s}}^{\mathrm{PMMA}}$ for the PMMA/steel bimaterial interface and about 130% of the upper extreme of $c_{\mathrm{s}}^{\mathrm{Homalite-100}}$ for the Homalite-100/aluminum bimaterial interface. Nevertheless, the dilatational wave speed of material 1 (PMMA or Homalite-100) was not exceeded in either case. Crack growth in this speed regime is termed as being *intersonic*.

Crack propagation in the intersonic regime has a direct effect on the nature of the fringe patterns observed. At first the fringes are smooth and continuous, while the crack-tip is still subsonic, as shown in the first few frames in figures 5 and 7. Moreover, the forward and rear fringe loops focus at a *single point* along the interface, which is the crack-tip. In subsequent frames, however, the fringes become squeezed and elongated normal to the interface. Finally, in the intersonic crack growth regime, the fringes in the centre of the two lobed fringe pattern do not seem to focus to a single point along the interface. Instead they intercept the bond line over a finite

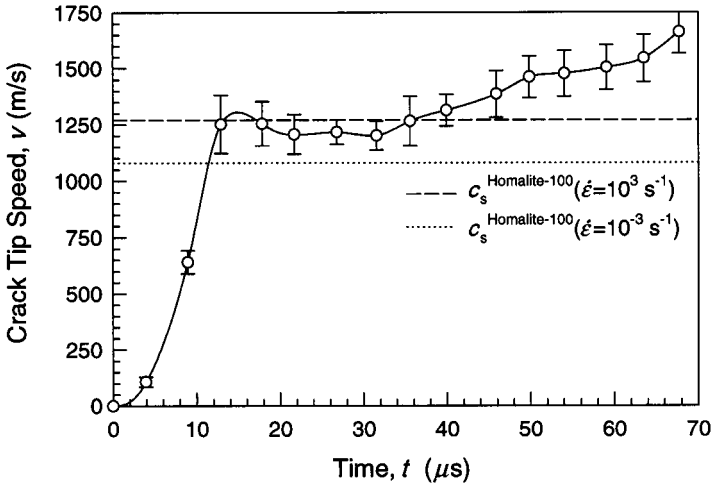

Figure 8. Typical crack-tip speed history for dynamic crack growth along a Homalite-100/aluminum bimaterial interface subjected to impact loading.

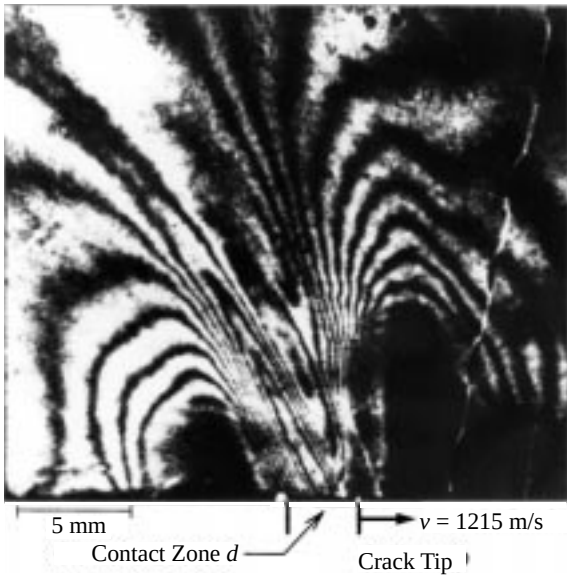

Figure 9. Enlarged view of CGS fringes in the intersonic crack growth regime showing the area of crack face contact.

area between the two main lobes, which is evident in the last frame in figure 5 and the last three frames in figure 7. This effect is seen clearly in figure 9, in which the length of the area between the front and back lobes is identified as d. The fringe pattern seen in this particular frame is caused by large-scale contact of the crack faces along d, as the crack is propagating in the intersonic regime. This large-scale contact of crack faces was first observed by Lambros & Rosakis (1995*c*), theoretically confirmed by Liu *et al.* (1995), and also observed by Singh & Shukla (1996). From the numerical simulation point of view, Xu & Needleman (1996) have confirmed the existence of a contact-zone area when the crack-tip speed exceeds the lower of the two Rayleigh wave speeds.

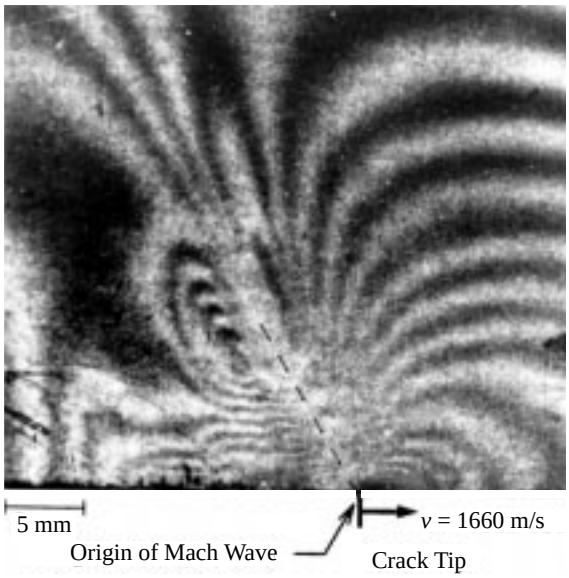

Figure 10. Discontinuities of isochromatic fringe contours representing the formation of a mach wave.

Another direct consequence of intersonic crack propagation is the formation of a mach wave (or line-of-discontinuity) in the stress field surrounding the moving crack-tip. The propagating crack-tip acts as a source of shear and dilatational stress waves which radiate out into the material and establish the stress field that surrounds the crack-tip. If this source (the crack-tip) propagates faster than the shear wave speed then the spreading out of the shear waves is limited and a mach wave (or line-of-discontinuity) forms. The existence of such mach waves was predicted by the analysis of Liu *et al.* (1995) but could not be confirmed by the earlier CGS experiments. Note that by the very nature of the technique, CGS would not be sensitive to these discontinuities in the stresses and hence the mach wave would not show up in the CGS interferograms. Experimental evidence of the mach wave is observed in the photoelasticity experiments in the form of discontinuous isochromatic fringe contours, as shown in figure 10. The line originates at the crack-tip and radiates out into the material.

(*b*) *Intersonic crack growth along an elastic/rigid interface*

It was noted earlier that both the PMMA/steel and Homalite-100/aluminum bimaterial systems can be modelled very well as elastic/rigid approximations. Now, consider a crack propagating intersonically along an elastic/rigid interface, as shown in figure 11. Using an asymptotic analysis Liu *et al.* (1995) have shown that the stress field around the crack-tip can be expressed as

$$\sigma_{ij} = \frac{\mu A_0}{1+\alpha_1^2\hat{\alpha}_s^2}\left\{\frac{\Sigma_{ij}^a}{r_1^q} + \frac{\Sigma_{ij}^b}{(\eta_1+\hat{\alpha}_s\eta_2)^q}H(\eta_1+\hat{\alpha}_s\eta_2) + \frac{\Sigma_{ij}^c}{(-\eta_1-\hat{\alpha}_s\eta_2)^q}H(-\eta_1-\hat{\alpha}_s\eta_2)\right\}, \tag{3.1}$$

$$\alpha_1^2 = 1-\frac{v^2}{c_1^2}, \quad \hat{\alpha}_s^2 = \frac{v^2}{c_s^2}-1, \tag{3.2}$$

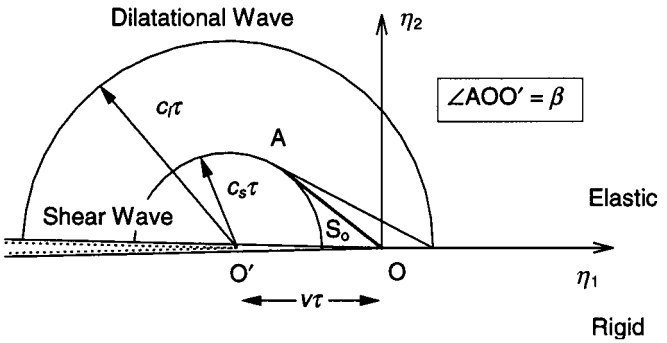

Figure 11. A crack propagating intersonically along an elastic/rigid interface.

where v is the crack-tip speed; μ, c_l and c_s are the shear modulus, dilatational wave speed and shear wave speed, respectively, of material 1 and $H(\cdot)$ is the Heaviside unit step function. Also, the functions Σ^a_{ij}, Σ^b_{ij} and Σ^c_{ij} are functions of θ_l, the crack-tip speed, v, and the wave speeds of material 1, c_l and c_s. The scaled polar coordinates are defined as

$$r_\mathrm{l} = \sqrt{\eta_1^2 + \alpha_\mathrm{l}^2\eta_2^2}, \quad \theta_\mathrm{l} = \arctan\left(\frac{\alpha_\mathrm{l}\eta_2}{\eta_1}\right). \tag{3.3}$$

Finally, the strength of the crack-tip singularity is given as

$$q(v) = \frac{1}{\pi}\arctan\left\{\frac{\alpha_\mathrm{l}\hat{\alpha}_\mathrm{s}[4-(1-\hat{\alpha}_\mathrm{s}^2)^2]}{4\alpha_\mathrm{l}^2\hat{\alpha}_\mathrm{s}^2 + (1-\hat{\alpha}_\mathrm{s}^2)^2}\right\}. \tag{3.4}$$

The variation of the singularity exponent, $q(v)$, with crack-tip speed, v, is plotted in figure 12 for different values of the Poisson's ratio of the elastic material. The exponent starts at a value of $q(v) = 0$ at $v = c_\mathrm{s}$ and increases monotonically with crack-tip speed till it reaches a maximum value at $v = \sqrt{2}c_\mathrm{s}$. With further increase in the crack-tip speed the exponent decreases monotonically back to the value $q = 0$. Note that $q(v)$ remains less than 0.5 for the entire speed range considered. This limit on the maximum value of $q(v)$ implies that energy flux into the moving crack-tip is always zero irrespective of the crack-tip speed in the intersonic crack growth regime.

The asymptotic analysis is very useful in explaining several key features of intersonic crack propagation along bimaterial interfaces. The first result is that across the head wave front S_0 (see figure 11) the components of stress and particle velocity are discontinuous. Therefore, unlike subsonic crack growth where only one singular point is present at the crack-tip, for the case of intersonic crack growth, an entire singular line of infinite jumps in stress and particle velocity appears in the body. The singularity across this line is the same as that at the crack-tip. The line originates from the propagating crack-tip and radiates out into the elastic solid. The existence of such a discontinuity is evident by inspection of equation (3.1) shown above. This is the line-of-discontinuity that appears in the isochromatic fringe patterns obtained in the photoelastic experiments. The equation of the moving line of discontinuity is given by

$$\eta_1 = \hat{\alpha}_\mathrm{s}\eta_2 = 0, \tag{3.5}$$

and thus, the angular orientation of this line, with respect to the interface, can be expressed in terms of the crack-tip speed, v, and the shear wave speed of the elastic

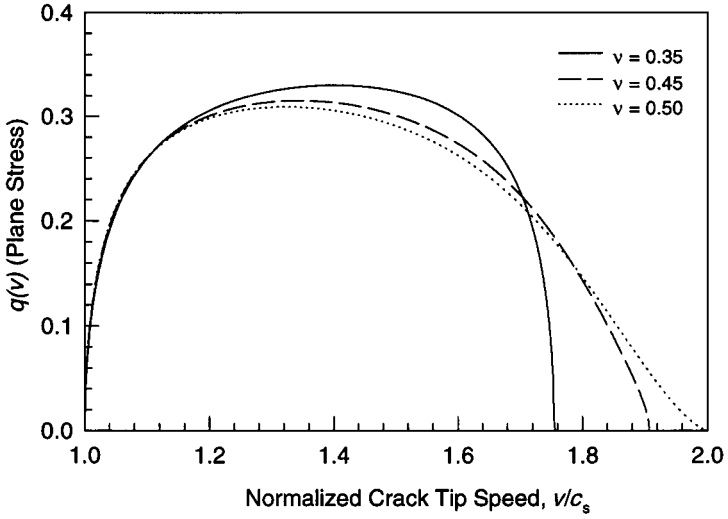

Figure 12. Variation of the singular exponent $q(v)$ as a function of crack-tip speed v for different values of Poisson's ratio (Liu *et al.* 1995).

Table 2. *Comparison of experimentally measured and theoretically predicted orientations of the line-of-discontinuity*

frame number	$v/c_{\mathrm{s}}^{\mathrm{Homalite-100}}$	β_{theory}	$\beta_{\mathrm{experiment}}$
13	1.16	59.5°	63°
14	1.19	57.5°	55°
15	1.21	55.7°	53°
16	1.30	50.3°	48°

material (or material 1), c_{s}, as

$$\tan\beta = \frac{1}{\sqrt{(v^2/c_{\mathrm{s}}^2) - 1}}. \tag{3.6}$$

The orientations of the line-of-discontinuity determined from the experimental isochromatic fringe patterns were compared with the angles predicted by the above equation and are listed in table 2. The correspondence between the experimentally observed and theoretically predicted angles is excellent and substantiates the fact that the experimentally observed line-of-discontinuity is indeed the theoretically predicted mach wave. Further evidence of the line-of-discontinuity is presented in the numerical simulations of Xu & Needleman (1996). Liu *et al.* (1995) also showed that there is no energy dissipation when the singular line S_0 moves through the elastic material.

Consider the normal tractions along the interface at an arbitrary distance a ahead of the moving crack-tip, $\sigma_{22}(a, 0^+, t)$, and the crack opening displacement at the distance a behind the moving crack-tip, $u_2(-a, 0^+, t)$. Then it can be shown (Liu *et al.* 1995) that if the crack-tip speed is in the range $c_{\mathrm{s}} < v < \sqrt{2}c_{\mathrm{s}}$, $\sigma_{22}(a, 0^+, t)$ and $u_2(-a, 0^+, t)$ have opposite signs. This implies that when the normal traction ahead of the crack-tip is positive, crack face penetration into the rigid substrate

is predicted. Now, positive normal tractions ahead of the crack-tip are required to facilitate interface rupture and crack face penetration is physically impossible. Hence, in the crack-tip speed range $c_s < v < \sqrt{2}c_s$ the crack faces would come into contact behind the propagating crack-tip. This accounts for the large scale contact of crack faces observed experimentally in the CGS interferograms when the crack-tip speed was indeed in the range $c_s < v < \sqrt{2}c_s^{PMMA}$. When the crack-tip speed is in the range $\sqrt{2}c_s < v < c_l$, a positive normal traction ahead of the crack-tip results in crack face opening behind the moving crack-tip and no contact of the crack faces should be observed. However, to date, no observations of crack-tip speeds greater than $\sqrt{2}c_s$ have been made.

It should be noted at this point that in the intersonic regime the asymptotic crack-tip field does not have the oscillatory nature characteristic of all subsonic crack growth solutions. In the subsonic cases it is this oscillatory nature that accounts for contact and interpenetration. As discussed by Rice (1988), in most cases, this 'small-scale' contact is of the order of $10^{-8}L$, where L is a characteristic length of the problem. The situation here is very different. The observed and predicted contact zones are large scale ($d \cong$ 1–5 mm) and are not a result of an oscillatory nature of the field. In the present scenario, contact is related to the intersonic motion of the crack-tip disturbance. Indeed this phenomenon is reminiscent of the intersonic motion of a line load on an elastic half-space. In this problem when the speed of the moving load exceeds the Rayleigh wave speed of the half-space the direction of surface displacements, under the load, is in opposition to the direction of loading as discussed by Georgiadis & Barber (1993).

When crack face contact does indeed occur, the asymptotic solution is no longer valid and the problem must be revisited under different crack face boundary conditions. Nevertheless, despite this limitation the solution does provide considerable conceptual insight into the intersonic crack-growth phenomenon.

The same qualitative observations as above have been made for a more realistic elastic/elastic analysis for intersonic bimaterial crack growth (Huang *et al.* 1996). Here again travelling mach waves have been predicted. Also, for certain crack-tip speed range large-scale contact was implied by the solution. However, the details of the speed range where contact is predicted is slightly modified depending on the relative magnitudes of wave speed mismatch of the two elastic solids.

Given the experimental observations presented in the previous section and the asymptotic analyses of Liu *et al.* (1995) and Huang *et al.* (1996) it is believed that when the crack-tip is propagating in the regime $c_s < v < \sqrt{2}c_s$, with respect to material 1, the crack faces behind the moving crack-tip would be in contact. This contact zone would propagate along with the moving crack-tip as illustrated in figure 13. To further investigate this phenomenon additional experiments were conducted using a slightly modified specimen geometry. These will be discussed in the following section.

(*c*) *Experiments with modified specimen geometry*

To further investigate the phenomenon of intersonic crack growth along a bimaterial interface another series of experiments was conducted using a wider specimen. This specimen was identical to the geometry shown in figure 3 except that it was twice as wide, which provides a longer path of propagation for the interface crack. This increased path of crack propagation allowed for a fuller development of the near-tip stress field in the intersonic regime. The increased width of the specimen also reduced the interaction of the propagating crack with the free boundaries of

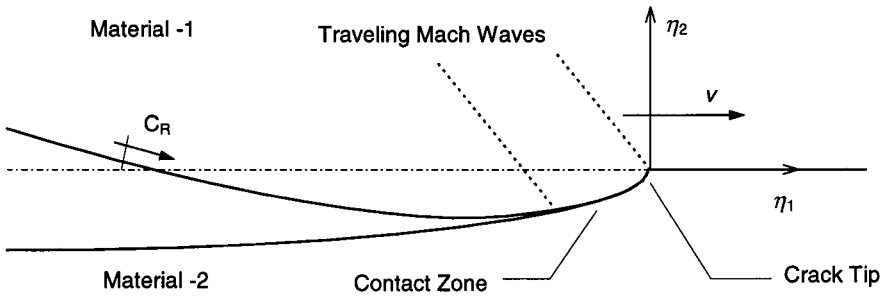

Figure 13. Schematic of crack face openings for a intersonically propagating interface crack.

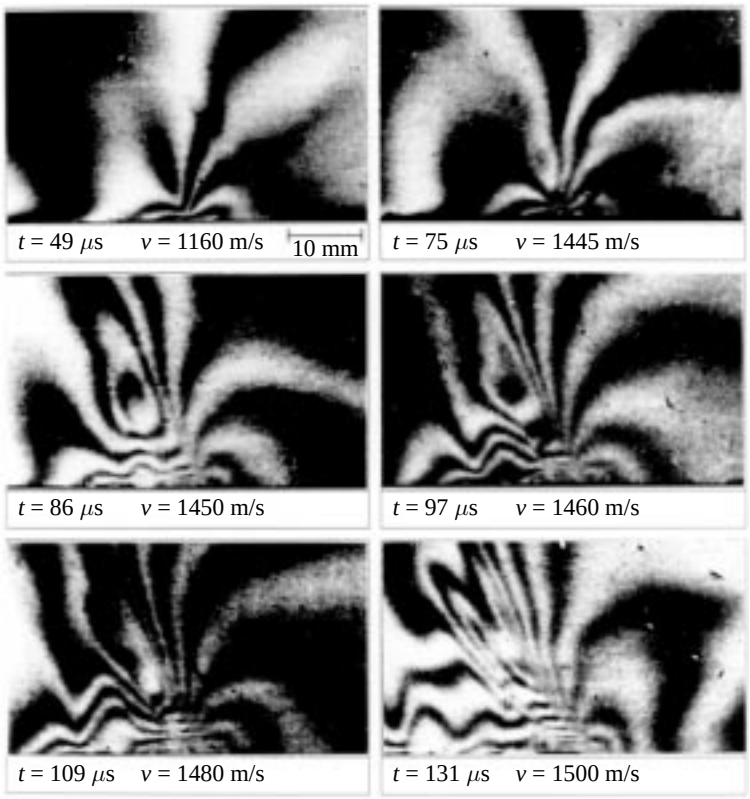

Figure 14. Typical set of isochromatic fringe patterns obtained for dynamic crack growth along a Homalite-100/aluminum bimaterial interface subjected to impact loading. (Wider specimen geometry).

the specimen. The net effect being that the intersonic regime could be explored in greater detail.

The specimen was impact loaded in the one point bend configuration, as before, and the failure process was observed using photoelasticity in conjunction with high-speed photography. In these experiments, only the technique of photoelasticity was employed since we were interested in observation of the line-of-discontinuity, which would not show up in CGS interferograms. Typical isochromatic fringe patterns obtained from one such experiment are shown in figure 14. The history of the crack-tip speed corresponding to this experiment is plotted in figure 15. As for the previous

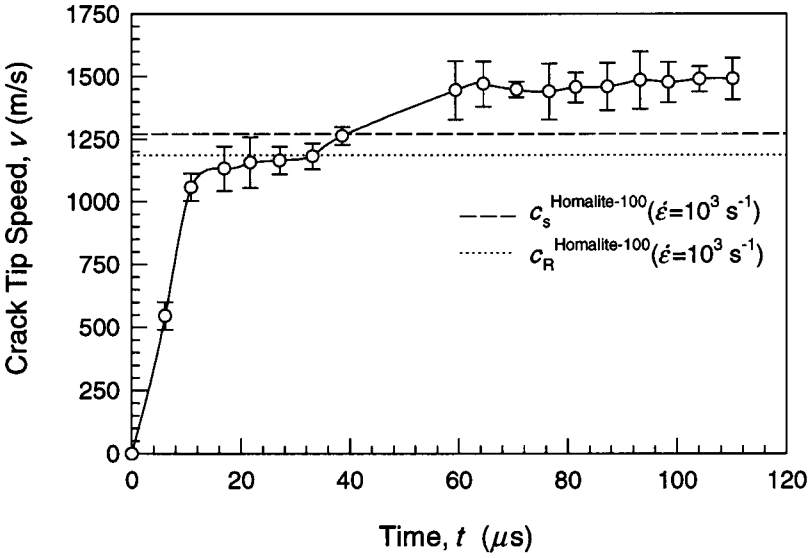

Figure 15. Typical crack-tip speed history for dynamic crack growth along a Homalite-100/aluminum bimaterial interface subjected to impact loading. (Wider specimen geometry).

experiments, the crack rapidly accelerated to the shear wave speed (upper extreme) of Homalite-100, $c_{\rm s}^{\rm Homalite-100}$. Thereafter, the speed accelerated further until it reached about 120% of $c_{\rm s}^{\rm Homalite-100}$. Subsequently, the crack-tip speed stabilized at this value and further propagation occurred in a 'steady-state' manner without any further crack-tip acceleration or deceleration.

As the crack-tip was propagating intersonically, the formation of a mach wave was observed in the form of a line-of-discontinuity emanating from the propagating crack-tip, as shown in figure 16. Also, since the crack-tip was propagating in the $c_{\rm s} < v < \sqrt{2}c_{\rm s}$ speed regime, large-scale contact of the crack faces was observed behind the moving crack-tip. This contact zone is characterized by fringes that run parallel to the interface, as shown in figure 16. A *secondary* mach wave was also observed in addition to the previously discussed mach wave (the *primary* mach wave that originated from the propagating crack-tip). The secondary mach wave originated from the trailing edge of the contact zone and represents the singularity that occurs when the crack faces separate at the end of the contact zone. The contact of the crack faces is a dynamic process, as this contact zone propagates along with the moving crack-tip. The trailing edge of the contact zone, as characterized by the secondary mach wave, was seen to propagate with the same speed as the moving crack-tip. Thus, the size of the contact zone remained relatively constant at around 2–3 mm during the 'steady-state' intersonic propagation phase of the interfacial crack-tip. This was further confirmed by the equal angles of inclination of the primary and secondary lines-of-discontinuity. Hence, this test confirms the mechanics of interfacial crack propagation in the $c_{\rm s} < v < \sqrt{2}c_{\rm s}$ crack-tip speed regime, as illustrated in figure 13.

The isochromatic fringe patterns in figure 14 also show the presence of another disturbance that follows the intersonically propagating crack-tip. This disturbance appears as a weak singularity, as shown in figure 16, and is produced when the crack-tip accelerates through the Rayleigh wave speed (upper extreme) of material 1 (Homalite-100). Thereafter, this singular disturbance trails the propagating crack-

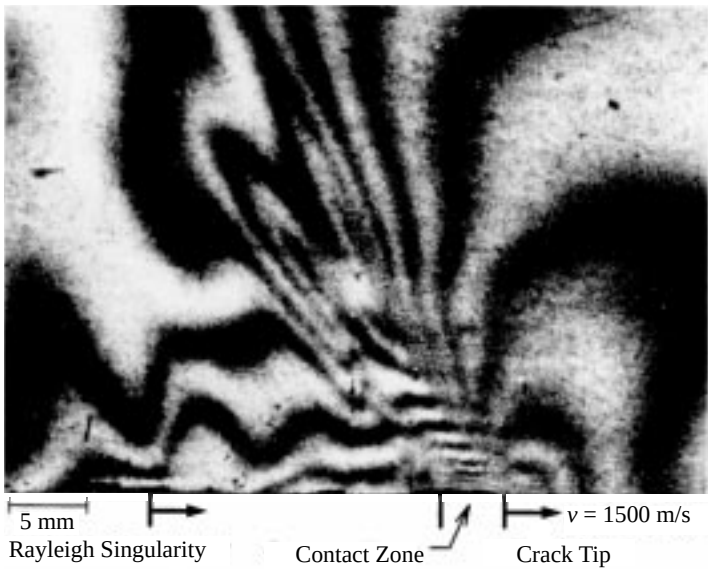

Figure 16. Details of the isochromatic fringe patterns around the intersonically propagating crack-tip showing the primary and secondary mach waves as lines-of-discontinuity, the dynamically moving contact zone and the Rayleigh disturbance.

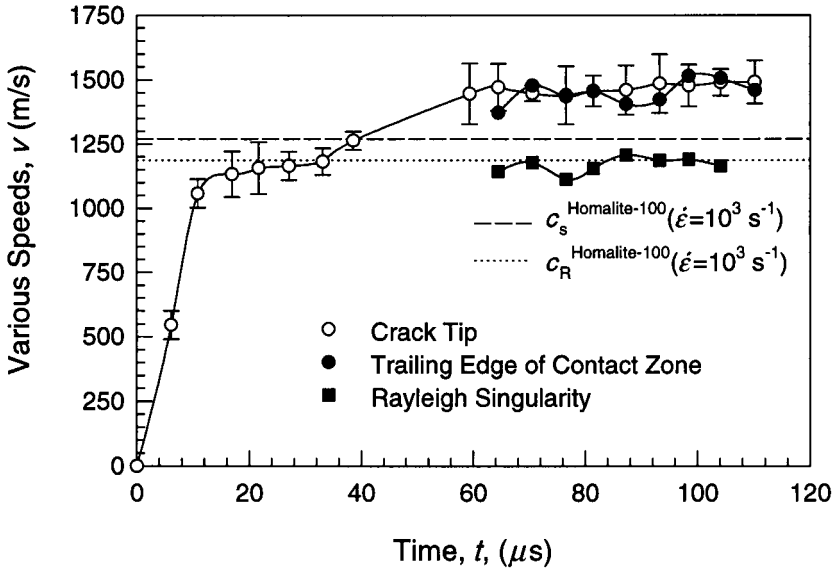

Figure 17. Histories of the speed of the propagating crack-tip, the trailing edge of the contact zone and the Rayleigh disturbance.

tip at the Rayleigh wave speed of material 1 (Homalite-100). Figure 17 shows the histories of the speeds of the interfacial crack-tip, the trailing edge of the contact zone, and the trailing Rayleigh wave singularity.

The history of the crack-tip speed shown in figure 15 clearly demonstrates that 'stable' crack propagation is possible in the $c_s < v < \sqrt{2}c_s$ regime. This is in contrast with the analysis of Liu *et al.* (1995) which postulates that this crack-tip speed regime is inherently unstable and the crack would accelerate beyond $\sqrt{2}c_s$. However,

the asymptotic analysis does not take into account the dissipation that would be introduced by the dynamically moving contact zone. It is believed that incorporating the energy dissipated by the propagating contact zone will shed greater light on the regimes of 'stable' intersonic crack propagation along bimaterial interfaces. Indeed since the crack-tip energy release rate is identically zero in this regime, frictional contact is the only mechanism of energy dissipation in the entire system. Note that the energy release rate is identically zero only from a linear elastodynamic viewpoint. Refinement of the theoretical model by incorporating a non-linear cohesive zone in the immediate vicinity of the propagating crack-tip would result in a small but non-zero energy release rate.

4. Closure

This paper describes the first experimental observations of various phenomena characteristic of dynamic intersonic decohesion of bimaterial interfaces. The optical techniques of coherent gradient sensing (CGS) interferometry and photoelasticity, were employed in conjunction with high-speed photography, in separate yet complementary experiments, to explore intersonic interfacial crack propagation in two different bimaterial systems, namely, PMMA/steel and Homalite-100/aluminum.

Using the two techniques the nature of large scale contact and mach wave formation at the vicinity of running cracks in the two bimaterial systems is explored. It is confirmed that large scale contact does indeed occur when the crack-tip speed is in the $c_s < v < \sqrt{2}c_s$ regime, as implied theoretically. Also, direct visual evidence is obtained for mach waves emanating from the intersonically moving crack-tip *and* the end of the intersonically moving contact zone.

The authors acknowledge the support of the National Science Foundation through a joint grant, no. CMS-9424113, to the University of Rhode Island and the California Institute of Technology (Dr O. Dillon, Scientific Officer). A.J.R. and J.L. also acknowledge the support of the Office of Naval Research under grant no. N00014-95-1-0453 (Dr Y. Rajapakse, Scientific Officer).

References

Aleksandrov, V. M. & Smetanin, B. I. 1990 Supersonic cleavage of an elastic strip. *PMM USSR* **54**, 677–682.

Archuleta, R. J. 1982 Analysis of near-source static and dynamic measurements from the 1979 Imperial Valley earthquake. *Bull. Seism. Soc. Am.* **72**, 1927–1956.

Broberg, K. B. 1960 The propagation of a Griffith crack. *Ark. Fys.* **18**, 159.

Broberg, K. B. 1985 Irregularities at earth-quake slip. *J. Tech. Phys.* **26**, 275–284.

Broberg, K. B. 1989 The near-tip field at high crack velocities. *Int. J. Fract.* **39**, 1–13.

Burridge, R. 1973 Admissible speeds for plane-strain shear cracks with friction by lacking cohesion. *Geophys. J. R. Soc. Lond.* **35**, 439–455.

Burridge, R., Conn, G. & Freund, L. B. 1979 The stability of a rapid mode II shear crack with finite cohesive traction. *J. Geophys. Res.* **85**, 2210–2222.

Bykovtsev, A. S. & Kramarovskii, D. B. 1989 Non-stationary supersonic motion of a complex discontinuity. *PMM USSR* **53**, 779–786.

Curran, D. R., Shockey, D. A. & Winkler, S. 1970 Crack propagation at supersonic velocities. II. Theoretical model. *Int. J. Fract.* **6**, 271–278.

Dally, J. W. & Riley, W. F. 1991 *Experimental stress analysis.* New York: McGraw-Hill.

Freund, L. B. 1979 The mechanics of dynamic shear crack propagation. *J. Geophys. Res.* **84**, 2199–2209.

Freund, L. B. 1990 *Dynamic fracture mechanics*. Cambridge University Press.

Georgiadis, H. G. & Barber, J. R. 1993 Steady-state transonic motion of a line load over an elastic half-space: the corrected Cole/Huth solution. *J. Appl. Mech.* **60**, 772–774.

Huang, Y., Liu, C. & Rosakis, A. J. 1996 Transonic crack growth along a bimaterial interface: an investigation of the asymptotic structure of near-tip fields. *Int. J. Solids Struct.* **33**, 2625–2645.

Lambros, J. & Rosakis, A. J. 1995*a* Dynamic decohesion of bimaterials: experimental observations and failure criteria. *Int. J. Solids Struct.* **32**, 2677–2702.

Lambros, J. & Rosakis, A. J. 1995*b* On the development of a dynamic decohesion criterion for bimaterials. *Proc. R. Soc. Lond.* A **451**, 711–736.

Lambros, J. & Rosakis, A. J. 1995*c* Shear dominated transonic interfacial crack growth in a bimaterial. I. Experimental observations. *J. Mech. Phys. Solids* **43**, 169–188.

Liu, C., Huang, Y. & Rosakis, A. J. 1995 Shear dominated transonic interfacial crack growth in a bimaterial-II. Asymptotic fields and favorable velocity regimes. *J. Mech. Phys. Solids* **43**, 189–206.

Liu, C., Lambros, J. & Rosakis, A. J. 1993 Highly transient elastodynamic crack growth in a bimaterial interface: higher order asymptotic analysis and experiments. *J. Mech. Phys. Solids* **41**, 1887–1954.

Rice, J. R. 1988 Elastic fracture mechanics concepts for interfacial cracks. *J. Appl. Mech.* **55**, 98–103.

Rosakis, A. J. 1993 Two optical techniques sensitive to gradients of optical path difference: the method of caustics and the coherent gradient sensor (CGS). *Exp. Tech. Fracture*, 327–425.

Singh, R. P. & Shukla, A. 1996 Subsonic and intersonic crack growth along a bimaterial interface. *J. Appl. Mech.* **63**, 919–924

Tippur, H. V. & Rosakis, A. J. 1991 Quasi-static and dynamic crack growth along bimaterial interfaces: a note on crack-tip field measurements using coherent gradient sensing. *Exp. Mech.* **31**, 243–251.

Tippur, H. V., Krishnaswamy, S. & Rosakis, A. J. 1991 A coherent gradient sensor for crack tip measurements: analysis and experimental results. *Int. J. Fract.* **48**, 193–204.

Winkler, S., Shockey, D. A. & Curran, D. R. 1970 Crack propagation at supersonic velocities. I. *Int. J. Fract.* **6**, 151–158.

Xu, X.-P. & Needleman, A. 1996 Numerical simulations of dynamic crack growth along an interface. *Int. J. Fract.* **74**, 289–324.

Yang, W., Suo, Z. & Shih, C. F. 1991 Mechanics of dynamic debonding. *Proc. R. Soc. Lond.* A **433**, 679–697.

Received 16 September 1996; revised 14 April 1997; accepted 12 June 1997